

N-th Nanoframes

Sungjae Yoo

Sungkyunkwan University

Jaewon Lee

Sungkyunkwan University

Hajir Hilal

Sungkyunkwan University

Insub Jung

Sungkyunkwan University <https://orcid.org/0000-0003-0827-9280>

Woongkyu Park

Korea Photonics Technology Institute (KOPTI)

Joong Wook Lee

Chonnam National University

Soobong Choi

Incheon National University

Sungho Park (✉ spark72@skku.edu)

Sungkyunkwan University

Article

Keywords:

Posted Date: March 18th, 2022

DOI: <https://doi.org/10.21203/rs.3.rs-1453659/v1>

License:   This work is licensed under a Creative Commons Attribution 4.0 International License.

[Read Full License](#)

Version of Record: A version of this preprint was published at Nature Communications on August 4th, 2022. See the published version at <https://doi.org/10.1038/s41467-022-32261-9>.

Abstract

Herein, we report unprecedented four-dimensional complex nanoparticles by embedding various kinds of three-dimensional polyhedral nanoframes within a single entity. This synthetic strategy is based on the selective deposition of metal atoms on high surface energy facets and subsequent growth into solid platonic nanoparticles, followed by the etching of inner metals, leaving complex nanoframes. Our synthetic routes are rationally designed and executable on-demand with a high structural controllability. Diverse Au solid nanostructures (octahedra, truncated octahedra, cuboctahedra, and cubes) evolved into complex multi-layered nanoframes with different numbers/shapes/sizes of internal nanoframes. We refer to the resulting four-dimensional complex nanoframes as “N-th nanoframes”. After coating the surface of the N-th nanoframes with plasmonically active metal (like Ag), the materials exhibited highly enhanced electromagnetic near-field focusing embedded within the internal complicated rim architecture.

Introduction

Four-dimensional (4D) complex nanoframes wherein multiple polyhedral nanoframes are integrated in a confined single entity are analogous to Kepler’s cosmic bowl, wherein the distance relationships between the six planets could be represented in terms of the five platonic solids enclosed within a sphere. Structurally, if polyhedral nanoframes are symmetrically arranged in a single entity, it will lead to extraordinary structural synergistic effects like highly efficient trapping of electromagnetic radiation within the sophisticated internal nanocavity. Such a complicated morphology would be ideal for a wide range of applications such as surface enhanced Raman scattering (SERS)¹, biosensors², catalysts³⁻⁵. Among various morphologies of nanostructures, nanoframes typically have a unique structural feature that can increase the accessibility of every surface in a given space, offering great potential for interactions with light and surface adsorbates. To date, enormous efforts have been devoted to improve the physicochemical properties of nanoframes⁶⁻¹⁸ by controlling the structural parameters such as shape, size, thickness, and composition. Nevertheless, all the nanoframes synthesized so-far are structurally simple and mainly composed of single-rim structures, limiting the utilization of inner voids, making it difficult to harness efficient structural coupling effects or light-matter interactions¹⁹⁻²³. In this regard, integrating multiple nanoframes in a single entity can be considered as a new paradigm for efficiently amplifying the structural characteristics of nanoframes. However, the synthetic strategies for complex nanoframes with different multiple internal geometries are rare, and the synthesis of complex multiple nanoframes in a controllable fashion (especially in a solution phase with a high yields and homogeneity in size and shape) remains a great challenge²⁴⁻³⁰. Herein, we develop rationally designed on-demand multi-step chemical reactions for 4D complex nanoframes with a high degree of structural controllability, which we denoted such unprecedented nanoframes as “N-th nanoframes”.

A schematic illustration (Fig. 1) of synthetic processes for N-th nanoframes exhibits the detailed multi-step routes to make each complex nanoframe. As a proof of concept, we show three distinctive pathways that are designed using different starting shapes of Au solid nanoparticles (such as octahedra, truncated

octahedra, and cubes, enclosed by only {111}, a combination of {111} and {100}, and only {100} facets, respectively) followed by on-demand combinations and multiple repetition of the several distinctive chemical toolkits. Each distinctive chemical reaction is described by arrows with different colors. These are listed as follows: (1) “Rim-selective growth of Pt” (blue arrows): Pt ions are preferentially reduced at the edge and vertex regions of Au solid nanoparticles. (2) “Well-faceted overgrowth of Au” (red arrows): Au atoms are deposited over the entire surface, retaining well-defined facets and evolving to platonic and truncated platonic nanoparticles. (3) “Selective etching of inner Au” (black arrows): Au atoms are selectively etched away, leaving mainly a Pt framework with residual Au. It is worth mentioning that multiple repetition of “well-faceted overgrowth of Au” step allows one to precisely modulate both the size and shape of Au nanostructure intermediates, resulting in multiple polyhedral nanoframes with tailorable structures. We denoted such unprecedented nanoframes as “N-th nanoframes”. To clearly differentiate each structure, we suggest a nomenclature of [Order-Composition-Shape-Morphology]. Order indicates the total number of nanoframes embedded in a single entity (e.g., 1st, 2nd, 3rd, and 4th). Composition implies the main element composing the nanostructure (e.g., Pt, Au, and Ag), and shape depicts each geometry starting from the core to the outer shape (e.g., octahedron (O), truncated octahedron (TO), cuboctahedron (CO), and cube (C)). The last abbreviation indicates if the material is composed of solid nanoparticles (NPs) or nanoframes (NFs).

By following the synthetic pathway shown in Fig. 1, we describe how one can synthesize “2nd -Pt-O-O-NFs” (Far-left scheme in Fig. 1). First, Au octahedral NPs with sizes of 48 ± 1 nm were employed as a starting template (Fig. 2A), and we applied “rim-selective growth of Pt” decorating edges and vertexes with Pt (Fig. 2B), “well-faceted overgrowth of Au” to enlarge octahedral NPs (Fig. 2C), and “rim-selective growth of Pt” again leading to 2nd -Au@Pt-O-NPs (Fig. 2D). In the first “rim-selective growth of Pt” step, Pt atoms are selectively deposited along the edges and vertexes of Au octahedral NPs because the relatively higher surface energy of those protruded sites can facilitate a galvanic replacement reaction between Pt^{4+} ions and the thin Ag layer coated on the entire surface of Au octahedral NPs, leading to 1st -Au@Pt-O-NPs with a total size of 77 ± 2 nm (Fig. 2B). In the “well-faceted overgrowth of Au” step, the morphologies of 1st -Au@Pt-O-NPs are transformed into solid 2nd -Au-O-NPs (100 ± 2 nm, Fig. 2C). The size of resulting solid 2nd -Au-O-NPs is tunable from 90 ± 2 nm to 111 ± 4 nm by simply controlling the amount of Au ions (Supplementary Fig. S1). This “well-faceted overgrowth of Au” step is an important intermediate step to allow subsequent chemical reaction (e.g., rim-selective growth of Pt) aided by formation of flattened surfaces and sharp edges via the Frank-van der Merwe mode as shown in Fig. 2E. In the nucleation and growth step of Au, Pt sites can act as nucleation sites in the presence of both Ag^+ ions and Cl^- ions and pre-formed thin Ag layers can induce the epitaxial growth of Au in a lateral direction, enlarging the flat Au terrace along the Au basal plane. To investigate the underlying mechanism of the “well-faceted overgrowth of Au” step, we controlled the experimental parameters such as counter anions, presence of Ag^+ ions, as well as the concentration of Au^{3+} ions. As shown in Supplementary Fig. S2, three different growth patterns of Au on the surface of 1st -Au@Pt-O-NPs were observed. As the concentration of Au ions increases, Au atoms are preferentially reduced on Pt regions in the presence of both Ag^+ ions and Cl^- ions (reaction condition 1), forming flattened surfaces and sharp edges via the

Frank-van der Merwe (FW) mode. As Au growth proceeds, edge domains expand with flattened facets in symmetric dual directions, and they are eventually merged, resulting in enlarged octahedral Au NPs with eight well-defined flat facets (as shown in Supplementary Figs. S2, B to D). In contrast, in the absence of Ag^+ ions (reaction condition 2), non-epitaxial growth of Au is observed, leading to Au nanoparticles with roughened surfaces following Stransky-Krastanov (SK) mode, as shown in Supplementary Fig. S2, E to G. In addition, when counter-anions changed to Br^- ions (reaction condition 3), indistinctively evolved dull edges were observed as shown in Supplementary Figs. S2, H to J, indicating that Cl^- ions play an important role in inducing the formation of thin Ag layers. This is caused by the higher reduction potential of AgCl complexes ($E^\circ/V = 0.22$ vs. Ag/AgCl) than that of AgBr complexes ($E^\circ/V = 0.07$ vs. Ag/AgCl). The presence of a thin layer of Ag is necessary to reduce the difference in lattice constant between Pt and Au (e.g., lattice constant of Au and Pt is 0.4065 nm and 0.3912 nm, respectively), leading to the epitaxial growth and formation of well-defined facets. As evidenced by EDS image mapping data (Supplementary Fig. S3), Ag atoms are preferentially deposited along the Pt sites, and the atomic percentages of Au, Pt, and Ag were 60%, 20%, and 20%, respectively. It should be noted that preferential deposition of Ag on the Pt sites results from the higher catalytic activity of the Pt surface compared to that of the Au surface. Additionally, the synthetic pathway can be expanded to other different shapes such as truncated octahedral and cube shapes, proving the general applicability of well-faceted overgrowth of Au (Supplementary Fig. S4). After applying the second “rim-selective growth of Pt” step, 2nd -Au@Pt-O-NPs with total size of 125 ± 4 nm could be obtained (Fig. 2D). Bright lines along the edge sites indicate that Pt atoms are selectively deposited on the edge regions. Finally, in the first “selective etching of Au” step, inner bulk Au domains were etched away through the comproportionation reaction of Au^+ ions, producing single Pt frameworks that have an octahedral shape and inner vacancy space (denoted as 1st -Pt-O-NFs) as shown in Figs. 2, F, G and J. Notably, after etching inner Au domains of 2nd -Au@Pt-O-NPs, Pt nanoframes with dual nanoframes (denoted as 2nd -Pt-O:O-NFs) were obtained as shown in Figs. 2, H, I and K. The 3D movie clip obtained with combined tilt series of TEM images taken from -60° to $+60^\circ$ angles (Supplementary Video 1) demonstrates that 2nd -Pt-O:O-NFs are composed of inner and outer nanoframes both with octahedral shapes, possessing intra-cavities connected via thin metal ligaments. Further, 1st -Pt-O-NFs and 2nd -Pt-O:O-NFs are mainly composed of Pt and a residual amount of Au confirmed by energy dispersive X-ray spectroscopy (EDS) in scanning transmission electron microscopy (STEM).

As shown in the synthetic pathway (middle scheme in Fig. 1), we applied a series of chemical reactions including multiple repetition of “well-faceted overgrowth of Au” to Au TO NPs bounded by {111} and {100} facets (Fig. 3). Au TO NPs with a total size of 55 ± 1 nm were utilized as a template (Fig. 3A) and applied for “rim-selective growth of Pt (1st -Au@Pt-TO-NPs)”, “well-faceted overgrowth of Au” (2nd -Au-TO-NPs), then again “rim-selective growth of Pt” (2nd -Au@Pt-TO-NPs), “well-faceted overgrowth of Au” (3rd -Au-O-NPs), and finally “rim-selective growth of Pt”, leading to 3rd -Au@Pt-O-NPs (Fig. 3, B to F, respectively). Notably, in the “selective etching of inner Au” step, inner Au domains of 1st, 2nd, and 3rd Au@Pt NPs were etched away, producing three kinds of complex nanoframes (denoted as 1st -Pt-TO-NFs (Fig. 3, G, H, and M), 2nd -Pt-TO:TO-NFs (Fig. 3, I, J, and N), and 3rd -Pt-TO:TO:O-NFs (Fig. 3, K, L, and O)). It is noteworthy

that in the first “well-faceted overgrowth of Au”, as the concentration of Au^{3+} ions gradually increases, the total size of the resulting structures increased from 90 ± 3 nm to 137 ± 5 nm and shape of intermediates of Au nanostructure can be precisely tuned from truncated octahedron to octahedron (Supplementary Fig. S5). Thereby, the outer shape of 2nd nanoframes could be controlled from truncated octahedral to octahedral nanoframes and the intra-nanogap distance between the inner and outer nanoframes of 2nd -Pt-TO:O-NFs was precisely tuned (Supplementary Fig. S6). Remarkably, the 3rd -Pt-TO:TO:O-NFs could be obtained wherein three different nanoframes are embedded in a single entity, namely, inner truncated octahedra, a middle truncated octahedral nanoframe, and the outer octahedral nanoframe, retaining intra-nanogaps regions among nanoframes, as shown in Fig. 3, K and L. Further, the 3D movie clip obtained with a combined tilt series of TEM images showed the structural details of 3rd -Pt-TO:TO:O-NFs, proving that three different nanoframes are beautifully overlapped in a 3D confined single entity (Supplementary Video 2).

Now, we suggest how to synthesize 4D N-th nanoframes with four different kinds of geometrical shapes, which illustrates the ultimate controllability of the resulting N-th nanoframes. The most significant morphology transformation of intermediates was observed when Au cubes enclosed by {100} facets were utilized as a starting material and four different complex nanoframes can be realized. The overall route to the 4th NFs is described in the far-right side of Fig. 1. Au cubes with total sizes of 30 ± 1 nm were employed as a starting material (Fig. 4A). Then, “rim-selective growth of Pt” and “well-faceted overgrowth of Au” were adopted multiple times. In the first “rim-selective growth of Pt” step, Pt atoms were selectively deposited on the edges of Au cubes, leading to 1st -Au@Pt-C-NPs (Fig. 4B). Subsequently, as the “well-faceted overgrowth of Au” and “Rim-selective growth of Pt” steps were applied repeatedly, both the shape and total size of intermediates of the Au nanostructure can be precisely modulated from 1st -Au@Pt-C-NPs with sizes of 40 ± 1 nm to Au cuboctahedra with sizes of 70 ± 1 nm (Fig. 4C, 2nd -Au-CO-NPs), Au truncated octahedra with a size of 98 ± 4 nm (Fig. 4E, 3rd -Au-TO-NPs), and Au octahedra with sizes of 136 ± 3 nm (Fig. 4G, 4th -Au- O-NPs). Notably, as “well-faceted overgrowth of Au” step proceeded, the shape transformed from cubes into cuboctahedra, truncated octahedra, and octahedra. Accordingly, the size evolved from 72 ± 2 nm to 142 ± 3 nm, as shown in Supplementary Fig. S7, B to H. Specifically, as Au overgrowth of 1st -Au@Pt-C-NPs gradually increased, eight vertex regions and six terrace regions were transformed into eight terrace regions and six vertex regions, respectively, leading to perfect octahedra (Supplementary Fig. S7). In the “selective etching of Au” step, inner bulk Au domains of the resulting 1st, 2nd, 3rd, and 4th Au@Pt NPs (Fig. 4, B, D, F, and H) were etched away to Au^+ ions, producing unprecedented complex nanoframes (denoted as 1st -Pt-C-NFs (Fig. 4, I, J, and Q), 2nd -Pt-C:CO-NFs (Fig. 4, K, L, and R), 3rd -Pt-C:CO:TO-NFs (Fig. 4, M, N, and S), and 4th -Pt-C:CO:TO:O-NFs (Fig. 4, O, P, and T), respectively). In addition, the outer shape of the double nanoframe could be controlled by tuning the degree of well-faceted overgrowth of Au, leading to 2nd -Pt-C:TO-NFs and 2nd -Pt-C:O-NFs (Supplementary Fig. S8). Remarkably, 4th -Pt-C:CO:TO:O-NFs were successfully obtained, wherein nanoframes with four different geometrical morphologies and sizes were integrated into a single entity, amplifying the extreme controllability of our synthetic strategies. Again, TEM tomography 3D movie clip measured from -60° to $+60^\circ$ angles (Supplementary Video 3) remarkably demonstrates that small cube

nanoframes are located in the center of the whole structures. Similarly, cuboctahedral, truncated octahedral, and octahedral nanoframes are contained in one 3D entity. It is noteworthy that low magnification SEM images (Figs. 4, I, K, M, and O) show a high degree of homogeneity in both shape and size, demonstrating the high controllability of our multi-step synthetic strategy.

To trap visible light inside N-th nanoframes, Ag atoms are deposited on the Pt scaffolds, leading to 4D complex Ag nanoframes with different numbers of inner nanoframes in a single entity (Supplementary Fig. S9). EDS analysis data show that a thin Ag layer was deposited on the entire surface while keeping their structural complexity (Supplementary Fig. S10). Typically, Ag atomic fractions of 1st, 2nd, 3rd, and 4th of Ag nanoframes were 35%, 30%, 42%, and 30%, respectively. The corresponding LSPR profiles of 1st, 2nd, 3rd, and 4th Ag nanoframes were obtained by ultraviolet–visible–near-infrared (UV–Vis–NIR) spectroscopy as shown in Fig. 5A, and single-particle surface-enhanced Raman scattering (spSERS) spectra are shown in Fig. 5B. We used 2-naphthalenethiol as an analyte for SERS measurements and a 633 nm laser (Laser power: 170 μ W) was used. Position of the individual N-th nanoframes was confirmed by Rayleigh scattering and SEM images (Supplementary Fig. S11). Remarkably, the representative spSERS signals show that the intensity of Raman signals is exponentially amplified as the number of inner nanoframes increases from singular- to quadruple-nanoframes in a single entity. (Figs. 5, B and C). In addition, SERS signals are obtained by measuring 40 single particles, indicating highly uniform and reproducible SERS signals (Supplementary Fig. S12). To systematically verify surface plasmon coupling phenomena of 4D complex Ag nanoframes with varying numbers of nanoframes, charge distribution plot data and electromagnetic near-field enhancement data were obtained by theoretical simulations based on a finite-element method (FEM) (Figs. 5, D and E). Charge distribution (red: electron rich, blue: electron deficient) clearly shows that the surface charge density significantly increased in a single entity as the number of nanoframes increased from single to quadruple, which is a distinctive characteristic of N-th nanoframes. We expect that surface plasmon coupling would occur in a complex manner, representing a broad LSPR feature (Fig. 5A). As shown in FEM field distribution images (Fig. 5E and Supplementary Fig. S13), 4th Ag nanoframes maximize the near-field focusing on those interstitial regions among nanoframes, wherein the adsorbed analytes would experience the strongly confined near-field, leading to highly amplified spSERS signals. As shown in Fig. 5C, the increased SERS signals were well correlated with the integrated field enhancement within N-th nanoframes.

Conclusion

Kepler tried to mimic the structure of the universe by ordering various solids (octahedron, icosahedron, dodecahedron, tetrahedron, and cube) in one entity. Likewise, N-th nanoframes allow multiple nanoframes of different geometries in a controlled way and mimic such a complicated arrangement in one nanoparticle. The synthetic chemical tools, executable on-demand in a customized way, lead to a high degree of homogeneity in both shape and size. The void space consists of many intertwined but separated nanorims, wherein the near-field focusing could be maximized, as verified by both spSERS measurements and theoretical calculations. There will be a myriad of future applications with these

unprecedented nanostructures, in the fields of catalysis, bio-analysis and therapeutics, optics, and electronics.

Methods

Synthetic Methods

Synthesis of Au Octahedral Nanoparticles

Au octahedral nanoparticles were synthesized by a seed-mediated method (21). To synthesize the Au seed solution, 600 μL of 10 mM of ice-cold NaBH_4 solution was injected into a mixture of 7 mL of 75 mM CTAB, 87.5 μL of 20 mM HAuCl_4 with vigorous mixing for 3 h. First, 6 mL of seed solution diluted 100 times was added to a solution containing 480 mL of 16 mM CTAB, 200 μL of 20 mM HAuCl_4 , and 6 mL of 0.1 M AA. The mixture was kept at 30°C for 12 h. Next, 210.8 mL of 100 mM CTAB, 1.4 mL of 20 mM HAuCl_4 , and 6.53 mL of 0.1 M AA were mixed in a round bottom flask, and 140.5 mL of first octahedral seed nanoparticle was added to the flask. The mixture was kept at 30°C for 4 h. The resulting solution was washed twice by centrifugation (8,000 rpm, 20 min).

Synthesis of Au Truncated Octahedral Nanoparticles

Au truncated octahedral nanoparticles were synthesized with a slight modification of the above method. First, to synthesize Au seed solution, 600 μL of 10 mM of ice-cold NaBH_4 solution was added to a mixture of 7 mL of 50 mM CTAB, 87.5 μL of 20 mM HAuCl_4 with vigorous stirring for 3 h. For the first growth process, 0.45 mL of seed solution diluted 100 times was added to a solution containing 12 mL of 16 mM CTAB, 25 μL of 20 mM HAuCl_4 , and 25 μL of 38.8 mM AA. The mixture was kept at 30°C for 12 h. For the second growth, 12 mL of the solution from the first growth process was added to a solution containing 12 mL of 16 mM CTAB, 3 mL of 2 mM HAuCl_4 , and 4.6 mL of 12 mM AA. After 5 min of reaction, the samples were centrifuged at 4,800 rpm for 30 min. This washing process was repeated two times.

Synthesis of Au Cubic Nanoparticles

Au cubic nanoparticles were synthesized as previously reported. (31) To synthesize the Au seed solution, 600 μL of 10 mM of ice-cold NaBH_4 solution was injected into a mixture containing 9.75 mL of 100 mM CTAB and 250 μL of 20 mM HAuCl_4 with stirring for 3 min. The solution was kept at 30°C for 3 h. Next, to synthesize 10 nm Au nanosphere, 2 mL of 200 mM CTAC, 2 mL of 0.5 mM HAuCl_4 , 1.5 mL of 0.1 M AA, and 50 μL of the CTAB-capped seed solution were added sequentially with stirring for 15 min. It was centrifuged twice and redispersed in 800 μL of 10 mM CTAC (14,500 rpm, 30 min). Finally, 20 mL of 100 mM CTAC, 100 μL of 10 nm Au nanospheres, 100 μL of 50 mM NaBr, 1.3 mL of 10 mM AA, and 20 mL of 0.5 mM HAuCl_4 were mixed with stirring for 30 min. The resulting solution was washed twice by centrifugation (8,000 rpm, 20 min).

Synthesis of 1st and 2nd Au@Pt Nanoparticles from Au Octahedral Nanoparticles: 1st and 2nd Au@Pt nanoparticles were fabricated via a stepwise manner using Au octahedra as seed particles. To synthesize 1st Au@Pt nanoparticles, 25 mL of 50 mM CTAB, 10 mL of Au octahedron (optical density: 1.2), 30 μL of 2 mM AgNO_3 , and 960 μL of 0.1 M AA were mixed in a vial in the presence of iodide ions (50 μM). After incubation at 70°C for 1 h, 960 μL of 0.1 M HCl and 300 μL of 2 mM H_2PtCl_6 were added to the solution and were incubated for 4 h. After the completion of the reaction, the solution was centrifuged twice at 8,000 rpm for 15 min. Before the 2nd deposition of Pt, well-faceted overgrowth of Au step was applied to the 1st -Au@Pt O-NPs. Specifically, 25 μL of 2 mM AgNO_3 , 2.5 μL of 0.1 M AA, and 25 μL of 2 mM HAuCl_4 was added to 250 μL of reaction solution consisting of 1st Au@Pt nanoparticles dispersed in CTAC, and the mixture was kept at 70°C for 1 h. The solution was centrifuged twice at 8,000 rpm for 5 min. Subsequently, Pt was deposited on the resulting nanoparticles. To accomplish this, 1 mL of 50 mM CTAB, 2 μL of 2 mM AgNO_3 , and 48 μL of 0.1 M AA were added to a 250 μL reaction solution containing the Au nanostructures obtained after well-faceted overgrowth of the Au step. After incubation at 70°C for 1 h, 48 μL of 0.1 M HCl and 20 μL of 2 mM H_2PtCl_6 were added and kept at 70°C for 4 h. After the reaction, the solution was centrifuged twice at 8,000 rpm for 5 min.

Synthesis of 1st, 2nd, and 3rd Au@Pt Nanoparticles from Au Truncated Octahedral Nanoparticles: To synthesize 1st, 2nd, and 3rd Au@Pt nanoparticles from Au truncated octahedral nanoparticles, Pt deposition and well-faceted overgrowth were applied to Au truncated octahedral nanoparticles repeatedly. For rim-selective deposition of Pt on Au nanoparticles, each reagent (described in table S1) was added in order. After adding AgNO_3 and AA, the solution was kept at 70°C for 1 h. Subsequently, 0.1 M HCl and 1 mM H_2PtCl_6 were added, and the solution was kept at 70°C for 4 h. The resulting solution was washed twice by centrifugation and redispersed in 1 mL of 0.2 M CTAC. For well-faceted overgrowth of Au, the pre-prepared Au nanostructures were dispersed in 1 mL of 0.2 M CTAC, and each reagent was added as described in table S2.

Synthesis of 1st, 2nd, 3rd, and 4th Au@Pt Nanoparticles from Au Cubic Nanoparticles: To synthesize 1st, 2nd, 3rd, and 4th Au@Pt nanoparticles from Au cube nanoparticles, Pt deposition and well-faceted overgrowth were performed repeatedly on Au truncated octahedral nanoparticles. For rim-selective deposition of Pt on Au nanoparticles, each reagent (described in table S3) was added in order. After adding AgNO_3 and AA, the solution was kept at 70°C for 1 h. Subsequently, 0.1 M HCl and 1 mM H_2PtCl_6 were added, and the solution was kept at 70°C for 4 h. The resulting solution was washed twice by centrifugation and redispersed in 1 mL of 0.2 M CTAC. For well-faceted overgrowth of Au, the pre-prepared Au nanostructures were dispersed in 1 mL of 0.2 M CTAC, and each reagent was added as described in table S4. After completion of the reaction, the mixture was washed twice by centrifugation (7,500 rpm, 5 min).

Synthesis of 1st, 2nd, 3rd, and 4th Pt Nanoframes: To selectively etch the interior Au domains of Au@Pt nanoparticles, 60 μL of 2 mM Au were added to 1 mL of CTAB-dispersed 1st, 2nd, 3rd, and 4th Au@Pt nanoparticles in the presence of 50 μM of iodide ions with gentle shaking. The mixed solutions were

incubated at 50°C for at least 1 h. The Pt nanoframes were collected by centrifugation twice and redispersed in 1 mL of 50 mM CTAC for further use.

Ag Deposition of 1st, 2nd, 3rd, and 4th Ag nanoframes: To deposit Ag, 30 μL of 50 mM NaOH, 30 μL of 2 mM AgNO_3 , and 30 μL of 10 mM AA were added to the CTAC-dispersed Pt nanoframe solution sequentially. The solution was kept at 30°C for 1 h and centrifuged twice after completion of the reaction.

Electric Field Simulations

For the electromagnetic simulation, finite element method (FEM) simulation was carried out using commercially-available software (COMSOL Multiphysics, Wave Optics Module). Studies were performed in 3D under the wavelength domain. The simulation domain was composed of nanoframe particle and water domain truncated using a perfectly matched layer (PML). In addition, the scattering boundary condition was also applied to avoid undesired scattering effects at the domain boundary. In the simulation, all geometric parameters were obtained from TEM. The nanoframes comprised gold (Au), silver (Ag), and platinum (Pt). The atomic ratio of each component was measured from EDS. The complex refractive index of each material was taken from the data of Johnson and Christy (32) or Rakić (33). In addition, the refractive index of water was assumed to be 1.33.

Single-particle SERS Measurement

The single-particle SERS measurement was conducted using a Raman microscope (Ntegra, NT- MDT) equipped with an inverted optical microscope (IX 73, Olympus). A dichroic mirror directs the excitation laser beam into an oil-immersion objective (UPlanSApo, 100 \times , 1.4 numerical aperture), which focuses the beam to a diffraction-limited spot ($\sim 2 \mu\text{m}$) on the upper surface of the cover glass slip. Photomultiplier tube images were obtained using a piezoelectric x, y sample scanner to identify nanoparticles. For attaching Raman reporter on the entire surface of nanostructures, we added the Raman reporter into solution including the resulting nanostructures and kept the solution at 30°C during 3h. After centrifugation twice, we can remove the extra amount of Raman reporter in solution and get the concentrated solution of nanostructure. Then, we dropped the solution on the cover glass and removed the droplet using blow gun after 5 min. The SERS spectra were acquired with 633 nm laser (He-Ne laser, Thorlabs) excitation for 10 s. The signals were obtained by a CCD detector (1024 \times 256 pixels; Peltier; cooled to -70°C, Andor Newton DU920P BEX2-DD). After analysis, FESEM images of the samples were obtained after Pt layer deposition using an Ar plasma sputter-coater (Cressington 108 auto) with a current level of 30 mA for 60 s on a slide glass.

Declarations

ACKNOWLEDGMENT

The authors are grateful to the Nam's lab in Seoul National University for providing a single-particle Raman spectroscopy. This research was supported by the Basic Science Research Program through the

National Research Foundation of Korea (NRF) grant funded by the Korean government (MSIT) (No. NRF-2021M3H4A4079145),

Author information

Author affiliations

Department of Chemistry, Sungkyunkwan University, Suwon 440-746, South Korea.

Sungjae Yoo, Jaewon Lee, Insub, Jung, Hajir Hilal, and Sungho Park

Department of Physics, Incheon National University; Incheon,155, Republic of Korea.

Soobong Choi

Medical & Bio Photonics Research Center, Korea Photonics Technology Institute (KOPTI); Gwangju, 61007, Republic of Korea

Woongkyu Park

Department of Physics and Optoelectronics Convergence Research Center, Chonnam National University; Gwangju 61186, Republic of Korea

Joong Wook Lee

Author contributions

S.Y., J. L., and H. H. performed the experiments and data analysis. S.Y. wrote the original draft and S. Y., S. P., I. J., and J. L. reviewed and edited the manuscript. W. P., S. C., and J. W. L. simulated FEM method for electromagnetic field enhancement. S.P. designed and supervised the project.

Competing interests

The authors declare no conflicts of interest.

Corresponding author

Correspondence to Sungho Park

Supplementary information

Supplementary Figs. 1 to 13, Tables 1 to 4, captions of video 1-3

References 31 – 33, Supplementary Videos 1 to 3

References

1. J. Langer *et al.*, Present and Future of Surface-Enhanced Raman Scattering. *Acs Nano*. **14**, 28–117 (2020).
2. Y. T. Yeh *et al.*, A rapid and label-free platform for virus capture and identification from clinical samples. *Proc. Natl. Acad. Sci. U. S. A.* **117**, 895–901 (2020).
3. Q. Wang, K. Domen, Particulate Photocatalysts for Light-Driven Water Splitting: Mechanisms, Challenges, and Design Strategies. *Chem. Rev.* **120**, 919–985 (2020).
4. A. Gelle *et al.*, Applications of Plasmon-Enhanced Nanocatalysis to Organic Transformations. *Chem. Rev.* **120**, 986–1041 (2020).
5. V. R. Stamenkovic, D. Strmcnik, P. P. Lopes, N. M. Markovic, Energy and fuels from electrochemical interfaces. *Nat. Mater.* **16**, 57–69 (2017).
6. A. Oh *et al.*, Skeletal octahedral nanoframe with Cartesian coordinates via geometrically precise nanoscale phase segregation in a Pt@Ni core-shell nanocrystal. *Acs Nano*. **9**, 2856–2867 (2015).
7. C. Chen *et al.*, Highly crystalline multimetallic nanoframes with three-dimensional electrocatalytic surfaces. *Science*. **343**, 1339–1343 (2014).
8. L. Zhang *et al.*, Platinum-based nanocages with subnanometer-thick walls and well-defined, controllable facets. *Science*. **349**, 412–416 (2015).
9. S. Chen *et al.*, Pd-Pt Tesseract for the Oxygen Reduction Reaction. *J. Am. Chem. Soc.* **143**, 496–503 (2021).
10. L. Xiong *et al.*, Octahedral gold-silver nanoframes with rich crystalline defects for efficient methanol oxidation manifesting a CO-promoting effect. *Nat. Commun.* **10**, 3782 (2019).
11. M. McEachran *et al.*, Ultrathin gold nanoframes through surfactant-free templating of faceted pentagonal silver nanoparticles. *J. Am. Chem. Soc.* **133**, 8066–8069 (2011).
12. S. Luo, P. K. Shen, Concave Platinum-Copper Octopod Nanoframes Bounded with Multiple High-Index Facets for Efficient Electrooxidation Catalysis. *Acs Nano*. **11**, 11946–11953 (2017).
13. Y. J. Xiong *et al.*, Corrosion-based synthesis of single-crystal Pd nanoboxes and nanocages and their surface plasmon properties. *Angew. Chem. Int. Edit.* **44**, 7913–7917 (2005).
14. N. Becknell *et al.*, Control of Architecture in Rhombic Dodecahedral Pt-Ni Nanoframe Electrocatalysts. *J. Am. Chem. Soc.* **139**, 11678–11681 (2017).
15. Z. Li *et al.*, Platinum-nickel frame within metal-organic framework fabricated in situ for hydrogen enrichment and molecular sieving. *Nat. Commun.* **6**, (2015).
16. Z. N. Wang *et al.*, Synthesis of Pd Nanoframes by Excavating Solid Nanocrystals for Enhanced Catalytic Properties. *Acs Nano*. **11**, 163–170 (2017).
17. X. Wang *et al.*, Pt-Based Icosahedral Nanocages: Using a Combination of {111} Facets, Twin Defects, and Ultrathin Walls to Greatly Enhance Their Activity toward Oxygen Reduction. *Nano Lett.* **16**, 1467–1471 (2016).
18. Y. E. Wu *et al.*, Sophisticated Construction of Au Islands on Pt-Ni: An Ideal Trimetallic Nanoframe Catalyst. *J. Am. Chem. Soc.* **136**, 11594–11597 (2014).

19. M. A. Mahmoud, M. A. El-Sayed, Gold nanoframes: very high surface plasmon fields and excellent near-infrared sensors. *J. Am. Chem. Soc.* **132**, 12704–12710 (2010).
20. L. Zhang *et al.*, Gold Nanoframes by Nonepitaxial Growth of Au on AgI Nanocrystals for Surface-Enhanced Raman Spectroscopy. *Nano Lett.* **15**, 4448–4454 (2015).
21. S. Yoo *et al.*, Three-Dimensional Gold Nanosphere Hexamers Linked with Metal Bridges: Near-Field Focusing for Single Particle Surface Enhanced Raman Scattering. *J. Am. Chem. Soc.* **142**, 15412–15419 (2020).
22. M. A. Mahmoud, W. Qian, M. A. El-Sayed, Following Charge Separation on the Nanoscale in Cu₂O-Au Nanoframe Hollow Nanoparticles. *Nano Lett.* **11**, 3285–3289 (2011).
23. W. S. Chew *et al.*, Nanoporous Gold Nanoframes with Minimalistic Architectures: Lower Porosity Generates Stronger Surface-Enhanced Raman Scattering Capabilities. *Chem. Mater.* **27**, 7827–7834 (2015).
24. S. Lee *et al.*, Particle-in-a-Frame Nanostructures with Interior Nanogaps. *Angew. Chem. Int. Ed. Engl.* **58**, 15890–15894 (2019).
25. M. Hajfathalian *et al.*, A Wulff in a Cage: The Confinement of Substrate-Based Structures in Plasmonic Nanoshells, Nanocages, and Nanoframes Using Galvanic Replacement. *ACS Nano*. **10**, 6354–6362 (2016).
26. J. Park *et al.*, Iridium-Based Multimetallic Nanoframe@Nanoframe Structure: An Efficient and Robust Electrocatalyst toward Oxygen Evolution Reaction. *ACS Nano*. **11**, 5500–5509 (2017).
27. X. Zhu *et al.*, Gold nanopyramid-embedded ultrathin metal nanoframes for in situ monitoring catalytic reactions. *Chem. Sci.* **11**, 3198–3207 (2020).
28. S. Yoo, J. Kim, S. Choi, D. Park, S. Park, Two-dimensional nanoframes with dual rims. *Nat. Commun.* **10**, 5789 (2019).
29. S. Yoo *et al.*, Silver Double Nanorings with Circular Hot Zone. *J. Am. Chem. Soc.* **142**, 12341–12348 (2020).
30. E. Gonzalez, J. Arbiol, V. F. Puntes, Carving at the Nanoscale: Sequential Galvanic Exchange and Kirkendall Growth at Room Temperature. *Science*. **334**, 1377–1380 (2011).

Figures

Surface energy of start materials

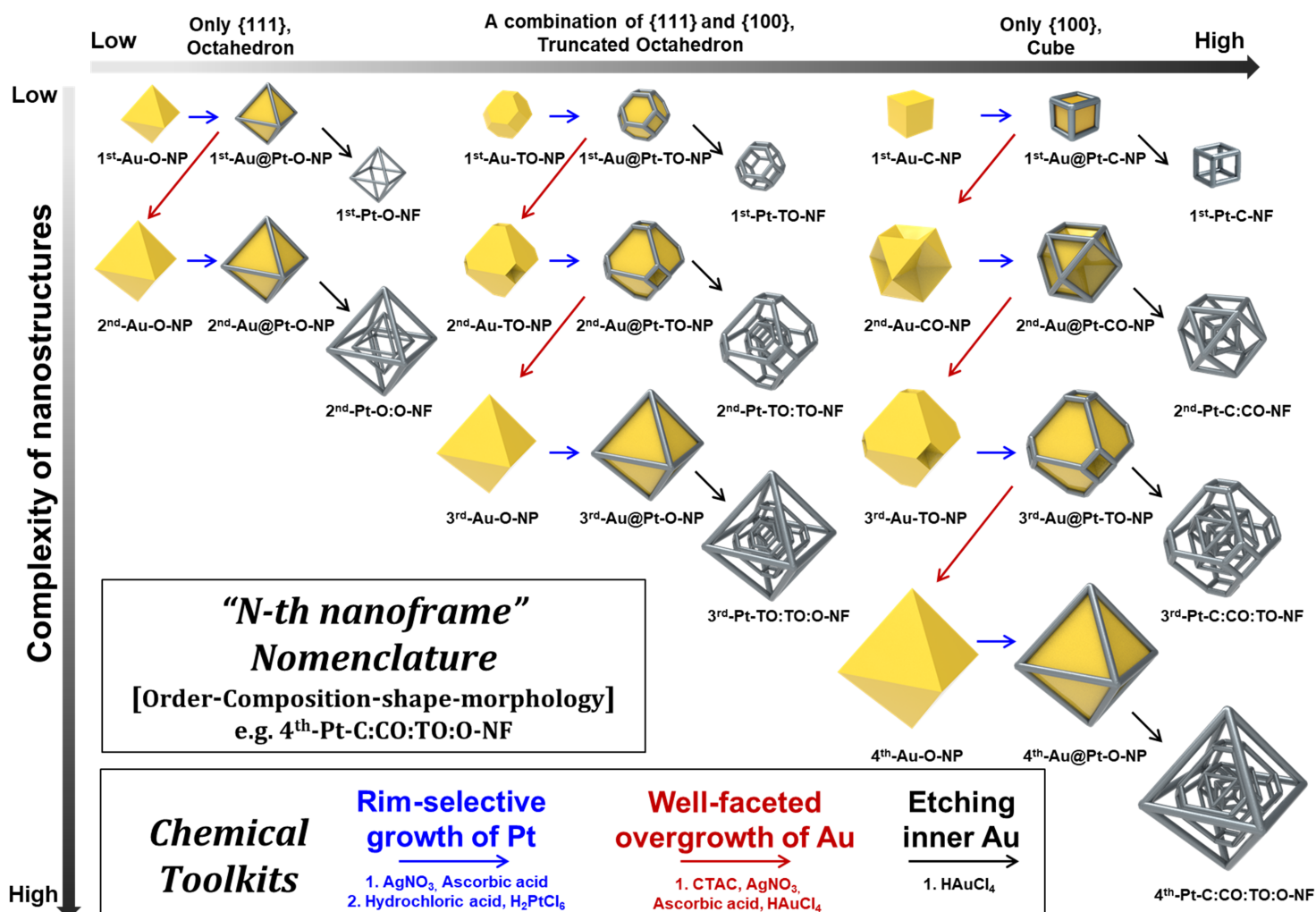


Figure 1

Schematic illustration of multi-step synthetic pathway for N-th nanoframes. Three distinctive synthetic pathways including rim-selective growth of Pt, well-faceted overgrowth of Au and etching inner Au are represented and the nomenclature for N-th nanoframes is suggested.

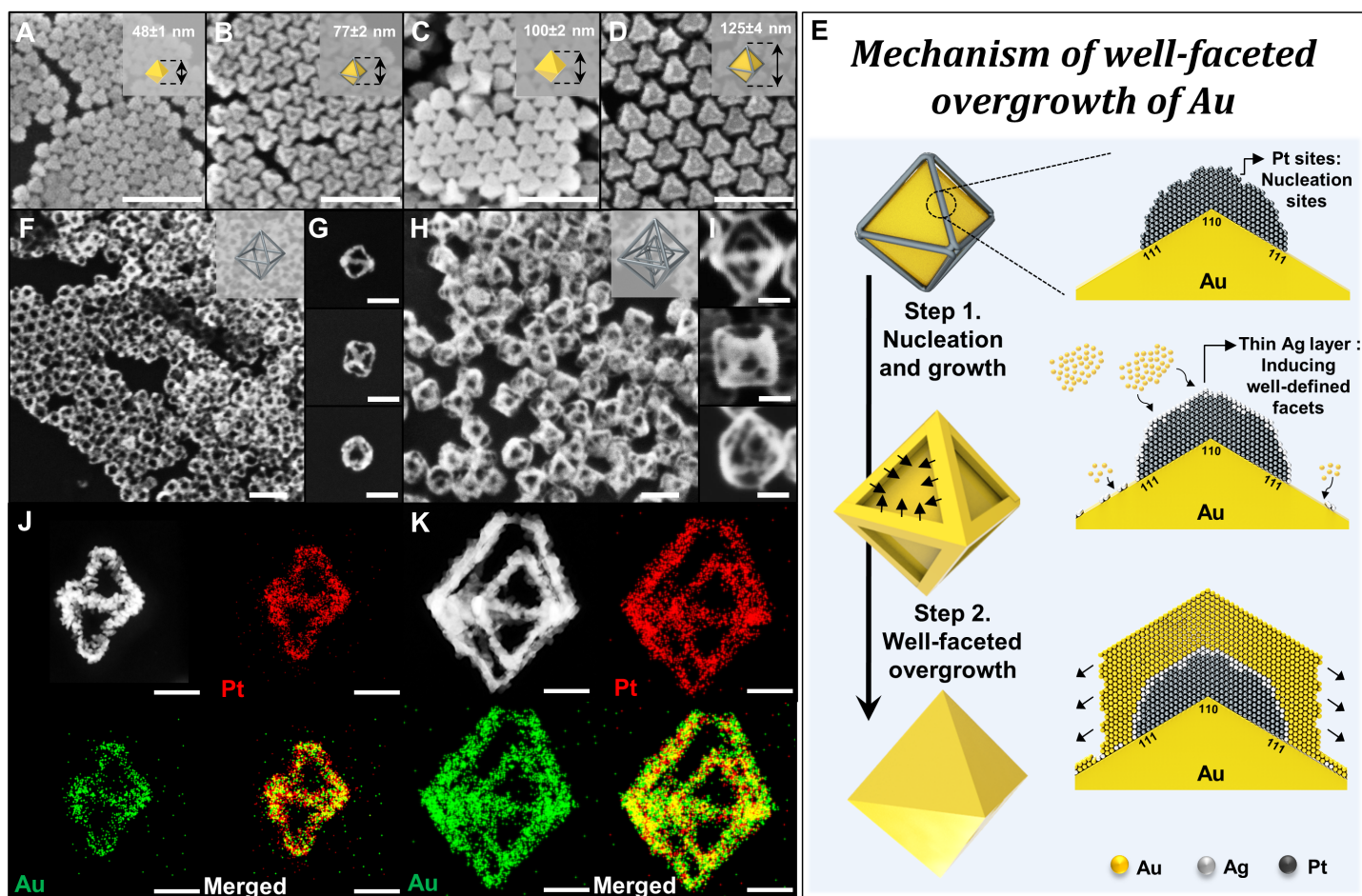


Figure 2

Representative schematic illustration for mechanism of well-faceted overgrowth of Au, and morphology evolution from 1st to 2nd nanoframes. (A to D) SEM images of (A) 1st-Au-O-NPs, (B) 1st-Au@Pt-O-NPs, (C) 2nd-Au-O-NPs, and (D) 2nd-Au@Pt-O-NPs, scale bar = 200 nm. (E) Schematic illustration that shows the mechanism of well-faceted overgrowth of Au. (F to I) Low magnification and zoomed-in SEM images viewed from <110>, <100>, and <111> directions of (F and G) 1st-Pt-O-NFs, and (H and I) 2nd-Pt-O:O-NFs, scale bar = 100 nm. (J and K) STEM images and EDS elemental mapping images of (J) 1st-Pt-O-NFs and (K) 2nd-Pt-O:O-NFs, scale bar = 30 nm.

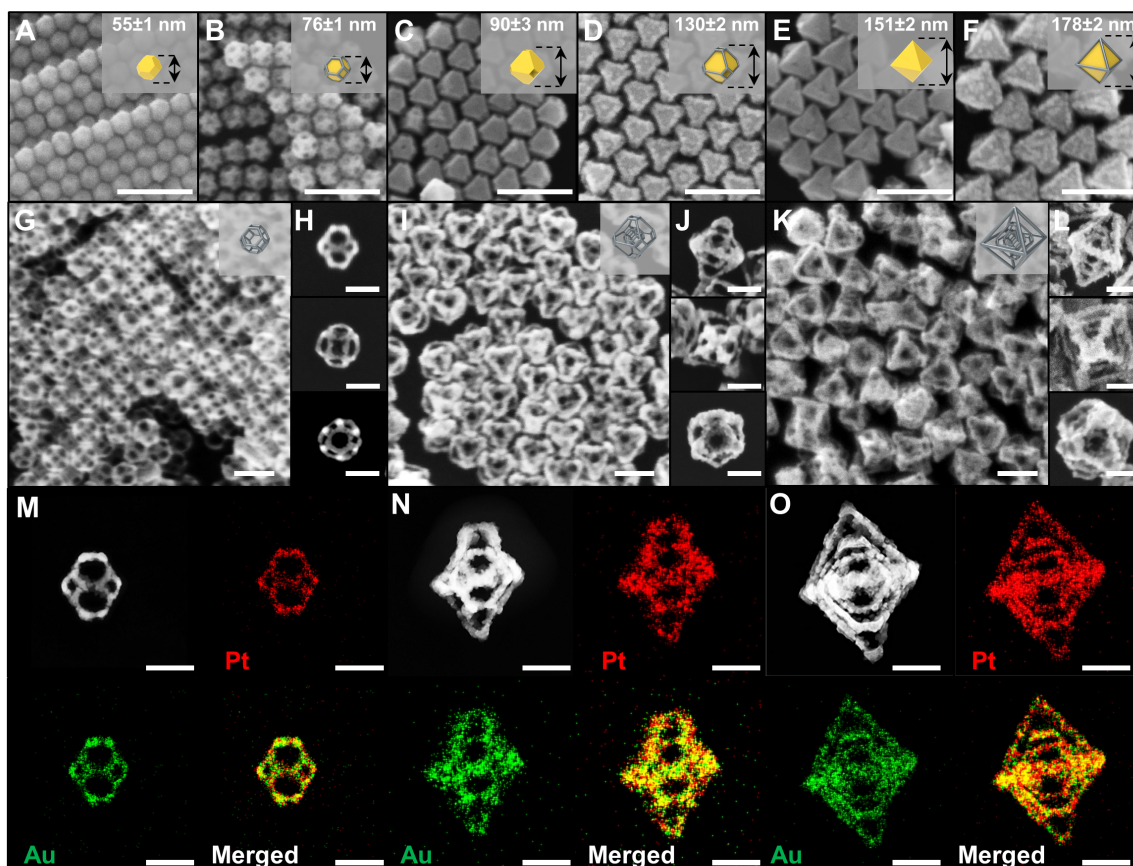


Figure 3

Morphology evolution from 1st to 3rd nanoframes. (A to F) SEM images of (A) 1st-Au-TO-NPs, (B) 1st-Au@Pt-TO-NPs, (C) 2nd-Au-TO-NPs, (D) 2nd-Au@Pt-TO-NPs, (E) 3rd-Au-O-NPs, and (F) 3rd-Au@Pt-O-NPs, scale bar = 200 nm. (G to L) Low magnification and zoomed-in SEM images viewed from <110>, <100>, and <111> directions of (G and H) 1st-Pt-TO, (I and J) 2nd-Pt-TO:O, (K and L) 3rd-Pt-TO:O:O NFs, scale bar = 100 nm. (M to O) STEM images and EDS elemental mapping images of (M) 1st-Pt-TO-NFs, (N) 2nd-Pt-TO:TO-NFs, and (O) 3rd-Pt-TO:TO:O-NFs, scale bar = 50 nm.

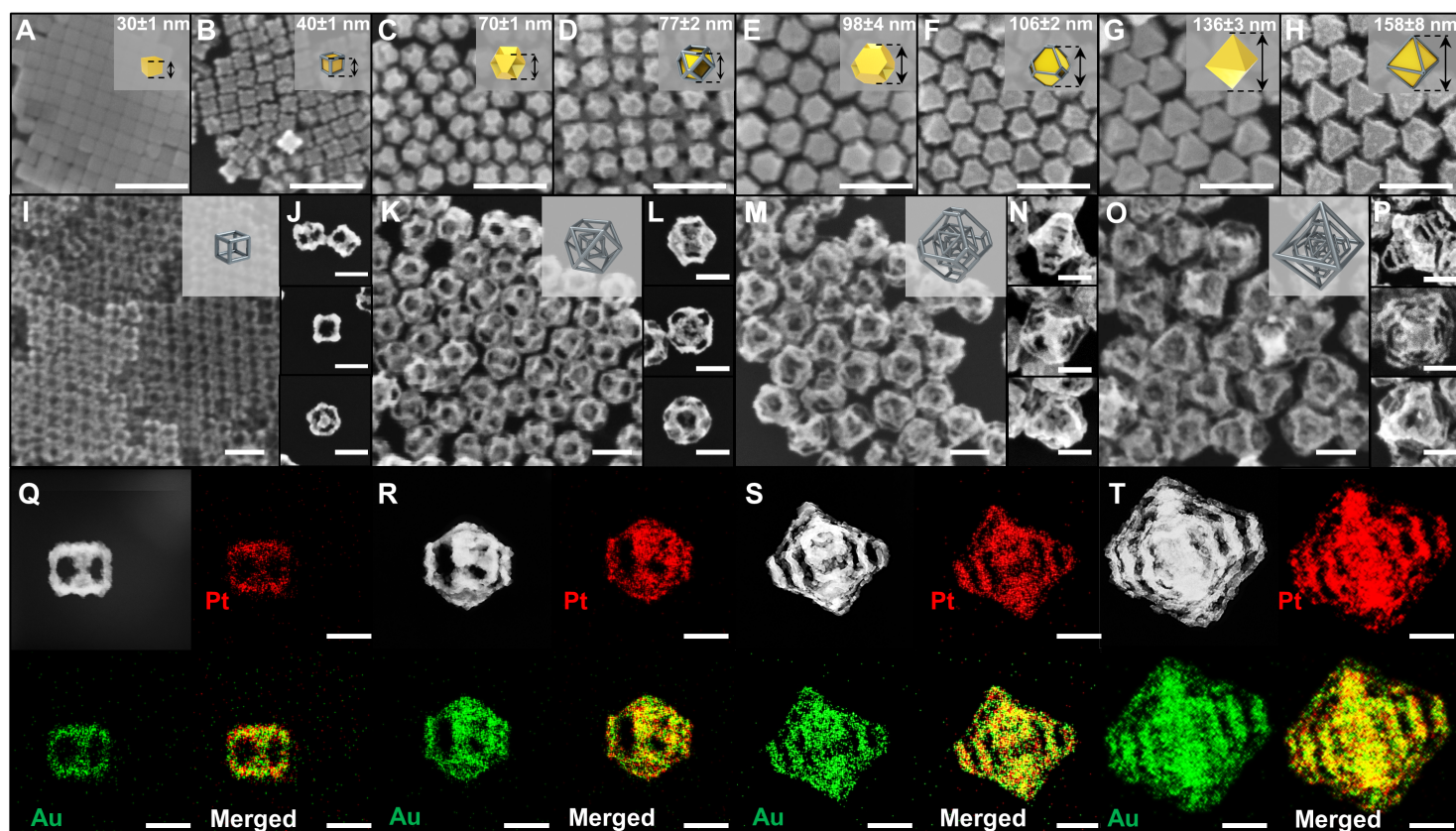


Figure 4

Morphology evolution from 1st to 4th nanoframes. (A to H) SEM images of (A) 1st-Au-C-NPs, (B) 1st-Au@Pt-C-NPs, (C) 2nd-Au-CO-NPs, (D) 2nd-Au@Pt-CO-NPs, (E) 3rd-Au-TO-NPs, (F) 3rd-Au@Pt-TO-NPs, (G) 4th-Au-O-NPs, and (H) 4th-Au@Pt-O-NPs, scale bar = 200 nm. (I to P) Low magnification and zoomed-in SEM images viewed from <110>, <100>, and <111> directions of (I and J) 1st-Pt-C-NFs, (K and L) 2nd-Pt-C:CO-NFs, (M and N) 3rd-Pt-C:CO:TO-NFs, (O and P) 4th-Pt-C:CO:TO:O-NFs, scale bar = 100 nm. (Q to T) STEM image and EDS elemental mapping images of (Q) 1st-Pt-C-NFs, (R) 2nd-Pt-C:CO-NFs, (S) 3rd-Pt-C:CO:TO-NFs, and (T) 4th-Pt-C:CO:TO:O-NFs, scale bar = 50 nm.

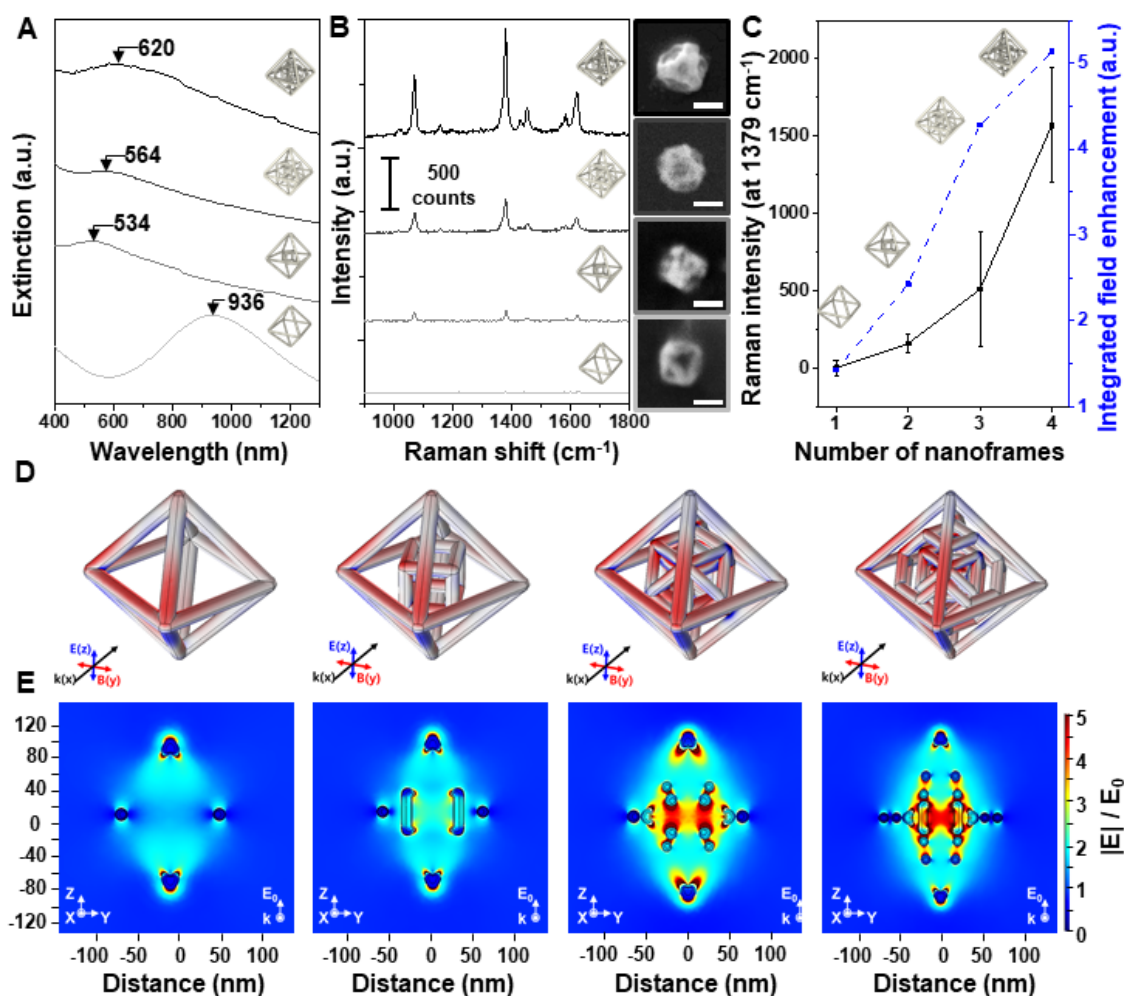


Figure 5

Investigating the optical properties of 4D complex Ag nanoframes with varying the number of nanoframes. (A) LSPR band profile of 1st, 2nd, 3rd, and 4th Ag nanoframes, (B) representative single-particle Raman signals of 1st, 2nd, 3rd, and 4th Ag nanoframes originating from their corresponding SEM images (scale bar = 200 nm), (C) plotted data of single-particle Raman intensity (at 1379 cm⁻¹) and theoretical calculated values of electric near-field enhancement as function of the number of nanoframes, (D) charge distribution and (E) near electromagnetic field contour maps (in the YZ cross-section) of 1st, 2nd, 3rd, and 4th Ag nanoframes with different numbers of nanoframes obtained by FEM simulation (Excitation wavelength: 633 nm).

Supplementary Files

This is a list of supplementary files associated with this preprint. Click to download.

- [SupplementaryInformation.docx](#)
- [VideoS12ndPtOONFs.mp4](#)
- [VideoS23rdPtTOTOONFs.mp4](#)
- [VideoS34thPtCCOTOONFs.mp4](#)